Liu, K.; Yang, S.; Li, W.; Wang, Y.; Sun, C.; Peng, L.; García Gómez, H. (2023). Non-noble-metal NiS promoted charge separation and photocatalytic hydrogen evolution for ZnCdS nano-islands on spherical SiO2. ACS Applied Energy Materials. 337. https://doi.org/10.1016/j.fuel.2022.126840

Non-noble-metal NiS promoted charge separation and photocatalytic hydrogen evolution for ZnCdS nano-islands on spherical SiO_2

Ke Liu [a,1], Shan Yang [a,1], Wei Li [a], Yifan Wang [a], Chuanzhi Sun [a,*], Lu Peng [b,*], Hermenegildo Garcia [b,*]

[a] College of Chemistry, Chemical Engineering and Materials Science, Shandong Provincial Key Laboratory of Clean Production of Fine Chemicals, Institute of Materials and Clean Energy, Shandong Normal University, Jinan 250014, PR China

[b] Instituto Universitario de Tecnología Química, Consejo Superior de Investigaciones Científicas-Universitat Politécnica de Valencia, Universitat Politecnica de Valencia Av, De los Naranjos s/n, 46022 Valencia, Spain

ARTICLEINFO

Keywords:
Hydrogen evolution
Synergistic effect
Visible light
SiO_2
NiS
ZnCdS

ABSTRACT

The efficiency of photocatalytic solar hydrogen evolution closely depends on the charge separation and the effective use of visible light. In this work, a highly efficient photocatalyst SiO_2/ZnCdS/NiS was synthesized through the self-assembly (ZnCdS loading to SiO_2) and photo-deposition method (NiS loading to ZnCdS). The synergistic effect of SiO_2 and NiS NPs can effectively promote photoelectron generation and separation, thereby enhancing photocatalytic performance. The hydrogen production activity of the efficient photocatalyst was as high as 8.4 mmol $g^{-1}h^{1}$ under visible light ($\lambda > 420$ nm), 8.4 times of SiO_2/ZnCdS, 4.4 times of ZnCdS/NiS and 2.6 times of SiO_2/ZnCdS/Pt. DFT calculations indicate that NiS, as a catalytic center, is beneficial for electron accumulation and further improves the hydrogen evolution. Meanwhile, loading of NiS to ZnCdS also improves the water adsorption capacity of photocatalyst, which is conducive to photocatalytic water decomposition.

1. Introduction

Since the photocatalytic decomposition of water over TiO_2 was firstly reported by Fujishima and Honda in 1972 [1], the photocatalytic hydrogen production from water has attracted widespread attention, mainly concerned with developing good photocatalysts [2–8]. An efficient photocatalyst should be with a suitable conduction band position to reduce H^+ to H_2, and a moderate band gap to absorb visible light. In addition, the photo-generated electrons and holes generated from the photocatalyst should be separated effectively. Meanwhile, good photocatalytic stability is also necessary. As a solid-state solution, ZnCdS has better properties than ZnS, CdS, and ZnS/CdS mixtures [9,10]. Through tuning the molar ratio of Zn and Cd, band edge positions for photo redox reactions and band gaps for light absorption of ZnCdS can be efficiently adjusted, and the best ratio has been achieved [11,12].

There are various preparation methods of photocatalyst, including coprecipitation, hydro/solvothermal treatment, etc. However, the prepared ZnCdS are prone to aggregation, which inhibits the transfer and separation of photogenerated electrons and holes [13–16]. Many advanced materials, such as reduced graphene oxide (rGO), metal–organic frameworks (MOFs), and graphitic carbon nitrides (g-C_3N_4) were employed to composite with ZnCdS. One of its most important functions is to eliminate the aggregation and thus decrease the particle size of ZnCdS to achieve better catalytic activity and stability [17–19]. Large area SiO_2 is a common support of nanoparticles (NPs). Excitingly, in addition to inhibiting the aggregation of oxide or sulfide, researchers reported that spherical SiO_2 can scatter light and make supported semiconductors generate more hot electrons [20,21]. Therefore, the spherical SiO_2 was selected as a carrier in the present photocatalytic system.

The addition of co-catalysts is an effective way to improve the photocatalytic activity of the semiconductor. Noble metals, such as Pt [22], Au [23], Ag [24], and Pd [25] have been widely used as co-catalysts to promote the separation and transfer of charges and surface reactions, while the scarcity and high cost extremely limit their large-scale application. Therefore, non-noble metals (Fe, Co, Ni, Mo) are much more promising [26–32]. Among them, Ni-based materials, especially NiS [33,34], attracted wide attention owing to their excellent performance

* Corresponding authors.
E-mail addresses: suncz@sdnu.edu.cn (C. Sun), lupen@doctor.upv.es (L. Peng), hgarcia@qim.upv.es (H. Garcia).
[1] K. Liu and S. Yang contributed equally to this work.

as co-catalysts [31,35].

Herein, a highly efficient photocatalyst SiO_2/ZnCdS/NiS was prepared through the photo-deposition method, which performs a hydrogen production activity of 8.4 mmol $g^{-1}h^{-1}$ and 2.6 times that of SiO_2/ZnCdS/Pt. The results indicate that the synergistic effect of SiO_2 enhancing light absorption and NiS NPs inhibiting electron-hole recombination and accelerating the charge transfer, both effects enhancing the photocatalytic performance. DFT calculations further suggest that NiS NPs, as reaction sites accumulate electrons, which can be subsequently be transferred to the H^+ from water, therefore promoting the H_2 evolution. In addition, loading of NiS to ZnCdS also improves the water adsorption capacity of photocatalyst, being conducive to photocatalytic water decomposition.

2. Experimental section

2.1. Photocatalysts preparation

Synthesis of SiO_2 spheres: SiO_2 spheres were prepared *via* the Stöber method. Briefly, 2 mL tetraethyl orthosilicate (TEOS) was added into a mixture with 40 mL isopropanol, 1 mL deionized H_2O and 2 mL $NH_3{\cdot}H_2O$ (10.5 M) under magnetic stirring. After reacting for 4 h at room temperature, the colloidal spheres were collected by centrifugation at 8000 rpm for 6 min and washed with DI water twice. Then, the sediment was dried at 60 °C to obtain SiO_2 spheres.

Surface modification of SiO_2 spheres: 0.1 g SiO_2 spheres were added in 30 mL deionized water followed by the ultrasound for 20 min. Then, ethylene diamine tetraacetic acid (EDTA) was added with constant stirring for 24 h at the temperature of 80 °C. After cooling to room temperature, the products were collected by centrifugation and washed with ethanol and deionized water for three times. Afterwards, the material obtained was dried at 60 °C for 12 h in air. The as-prepared sample was named as SiO_2/EDTA. As shown in Table S1, the zeta potential of SiO_2 spheres changed from −41.2 mV to 57.2 mV after the modification with EDTA.

Synthesis of SiO_2/ZnCdS composites: SiO_2/ZnCdS was prepared by a facile water bath reaction. Typically, 0.1 g SiO_2/EDTA was added in 30 mL deionized water followed by the ultrasound for 20 min. Then, a certain amount of cadmium acetate and zinc acetate was dissolved in the above solution with continuous stirring. After the two metal salts were completely dissolved, quantitative thioacetamide (50 % excess to stoichiometric amounts of cadmium acetate) was added into the above suspension, the mixture was put into an 80 °C water bath for 6 h with constant stirring. After cooling to room temperature, the products were collected by centrifugation and washed with ethanol and deionized water for three times, and then dried at 60 °C for 12 h in air. Similarly, the pure ZnCdS was prepared without the addition of SiO_2/EDTA.

Synthesis of SiO_2/ZnCdS/NiS composite photocatalysts: SiO_2/ZnCdS/NiS and SiO_2/ZnCdS/Pt were prepared by the photodeposition method. Specifically, the as-prepared SiO_2/ZnCdS (0.02 g) was dispersed in an 8 mL aqueous solution. Then, nickel acetate aqueous solution (1 mL) and thiourea aqueous solution (1 mL) with different concentrations were added. Afterwards, gases in the system were evacuated and the suspension was irradiated with a 300 W Xe lamp for 1 h under ultraviolet–visible (UV–vis) light. After that, the product was filtered and washed with distilled water and ethanol. The obtained material was dried at 60 °C overnight in a vacuum. Different from SiO_2/ZnCdS/NiS, SiO_2/ZnCdS/Pt was prepared from a 10 mL suspension of 0.02 g SiO_2/ZnCdS, 10 vol% triethanolamine (TEOA) and a certain amount of H_2PtCl_6. Then, gases in the system were removed through the vacuum and suspension was irradiated for 30 min under UV–vis light (300 W Xe lamp).

2.2. Characterizations

X-ray diffraction (XRD) patterns of samples were recorded on a Philips X′ pert Pro diffractometer with Cu Kα radiation (λ = 0.15418 nm). The Brunauer-Emmett-Teller (BET) specific surface areas of samples were measured by using a Micromeritics ASAP-2020 analyzer at 77 K. The high-resolution transmission electron micrographs (HRTEM) of the samples were obtained by using a JEM-2100 transmission electron microscope at an acceleration voltage of 200 kV. A Escalab 250 Xi (Thermo Scientific) X-ray photoelectron spectrometer with an Al-Kα X-ray (hν = 1486.6 eV) was used to perform X-ray photoelectron spectroscopy (XPS) analysis. The binding energy values obtained in XPS analysis were corrected by the C 1 s peak of 284.6 eV. UV–vis absorption spectra were measured by a UV–visible spectrometer (X-3, YuanXi Instruments). Photoluminescence (PL) spectra were recorded by using a FLS-980 Edinburgh fluorescence spectrophotometer. Transient photocurrent response and electrochemical impedance spectroscopy (EIS) spectra were measured on a CHI-660C electrochemical workstation with a standard three-electrode system. The three-electrode configuration includes a working electrode, a platinum plate as a counter electrode, and Ag/AgCl (saturated KCl) as a reference electrode. The light source was a 300 W xenon lamp with a 420 nm cutoff filter and the electrolyte solution was 0.1 M Na_2SO_4 solution. Transient photocurrent response and EIS were measured at 0.5 V (vs Ag/AgCl). 10 μL 0.25 % Nafion was added into 2 mL ethanol solution with 2 mg sample dispersed, followed by sonication for 30 min to form a slurry. The suspension was dropped onto a conductive glass (FTO) sheet (1 cm × 2 cm) and dried in an oven at 100 °C for 10 h to obtain the working electrodes. Electron paramagnetic resonance (EPR) signals were recorded on a Bruker A300-10/12/S-LC spectrometer with 2-methyl-N-(4-pyridinylmethylene)-2-propanamine N, N′-dioxide (POBN) as a trapping agent.

2.3. DFT calculation

In this study, all the DFT calculation was carried out with the Vienna Ab initio Simulation Package (VASP) version 5.4.4, projector augmented wave (PAW) method and the Perdew-Burke-Ernzerhof (PBE) function. The electron wave function is expanded by a plane wave with the kinetic energy cutoff of 350 eV. The convergence accuracy of energy values and atomic force were set as 1×10^{-6} eV and 0.02 eV/Å, respectively. A 2 × 2 × 1 Monkhorst-Pack k-point mesh was used to model ZnCdS and ZnCdS/NiS. The most stable configuration after optimization is shown in Figure S1. In order to accurately describe the nonnegligible van der Waals forces, van der Waals (vdW) correction was applied in all the calculations *via* the DFT-D3 method.

2.4. Photocatalytic hydrogen evolution test

The photocatalytic hydrogen production system was performed in a quartz flask. 5 mg photocatalyst was dispersed in an aqueous solution (8 mL H_2O and 2 mL triethanolamine) by magnetic stirring. Gases in the system were evacuated, and then, the photocatalytic system was irradiated with a 300 W Xe arc lamp with an ultraviolet cutoff filter (λ > 420 nm) under magnetic stirring. The hydrogen production is analyzed by a gas chromatograph (GC-7900, TCD, Ar as the carrier gas and 5 Å molecular sieve column.).

The external quantum efficiency (EQE) was measured at 405 nm, 420 nm, 450 nm and 500 nm monochromatic wavelength, respectively, by using a 300 W Xe lamp with a monochromator. The output intensities were determined by a NOVA II laser power meter (Ophir Photonics). The distance between the light source and the catalytic reaction device is 5 cm. And the EQE was calculated through the following Eq. (1):

$$EQE = \frac{\text{number of reacted electrons}}{\text{number of incident photons}} * 100\% = \frac{\text{numberofevolved}H_2\text{molecules} * 2}{\text{numberofincidentphotons}} * 100\% \quad (1)$$

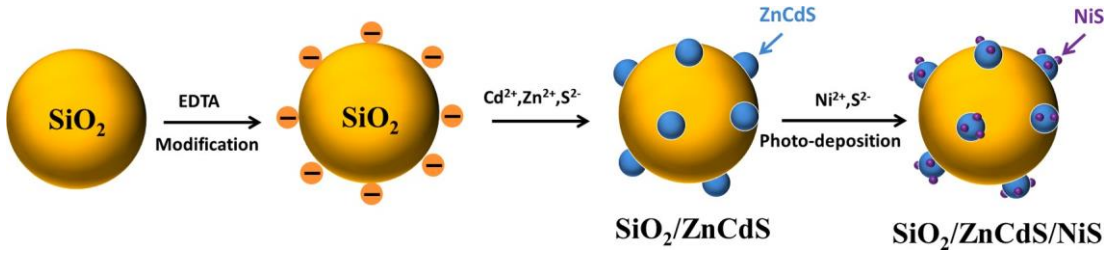

Scheme 1. Schematic illustration of the synthesis process of the SiO_2/ZnCdS/NiS.

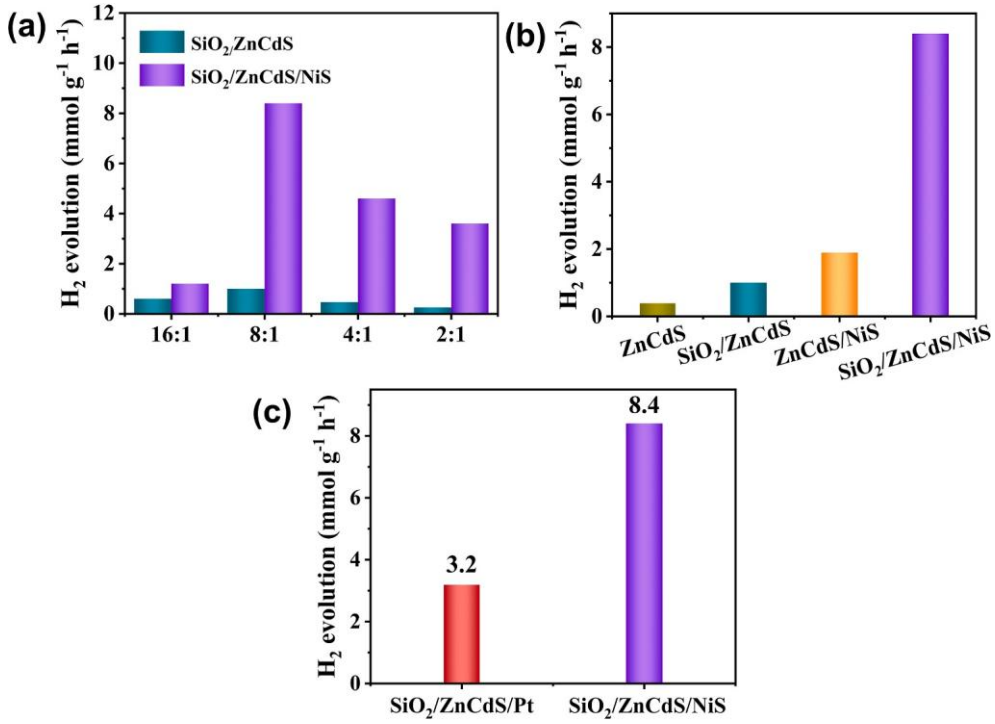

Fig. 1. (a) Photocatalytic H_2 production activity of SiO_2/ZnCdS and SiO_2/ZnCdS/NiS with different mass ratios of SiO_2 and ZnCdS. (b) Photocatalytic H_2 production activity of different samples. (c) Photocatalytic H_2 production of the SiO_2/ZnCdS/NiS photocatalyst compared with SiO_2/ZnCdS/Pt.

3. Results and discussion

Scheme 1 illustrates the synthesis of SiO_2/ZnCdS/NiS. SiO_2 spheres were firstly modified by ethylenediaminetetraacetic acid (EDTA) to generate highly negative charges on the surface. As shown in Table S1, the zeta potential of SiO_2 spheres changed from −41.2 to 57.2 mV after the modification of EDTA. Therefore, the subsequently added positively charged Zn^{2+} and Cd^{2+} were strongly adsorbed on the surface of SiO_2 spheres by electrostatic attraction, while S^{2-} released from thioacetamide slowly combines with metal ions, forming ZnCdS dotted on the surface of SiO_2 spheres. Afterwards, aqueous nickel acetate and thiourea solutions at different concentrations were added into the suspension of SiO_2/ZnCdS. The final SiO_2/ZnCdS/NiS was obtained through a photodeposition method.

3.1. Photocatalytic activity for H_2 evolution

Fig. 1 shows the H_2 production rates of different photocatalysts under visible light irradiation ($\lambda > 420$ nm). As shown in Fig. 1a, hydrogen production activity of SiO_2/ZnCdS and SiO_2/ZnCdS/NiS with different mass ratios of SiO_2 and ZnCdS were studied, in which the catalyst with a SiO_2 and ZnCdS mass ratio of 8 shows the highest H_2 production activity. For the SiO_2/ZnCdS ratio of 8, the H_2 production activity of SiO_2/ZnCdS is 1 mmol $g^{-1}h^{-1}$, and the activity of SiO_2/ZnCdS/NiS reaches 8.4 mmol $g^{-1}h^{-1}$. Figure S2 shows the influence of the concentration of nickel acetate precursors (used to prepare catalyst) on the performance of photocatalyst. When the concentration of nickel acetate is 1 mg mL^{-1}, the activity of the as-prepared catalyst is the highest. As shown in Fig. 1b, the H_2 production rate of pure ZnCdS is only about 0.4 mmol $g^{-1}h^{-1}$. While the H_2 production rate increases to 1.0 mmol $g^{-1}h^{-1}$ after supporting ZnCdS on SiO_2 spheres. In addition, the H_2 production rate of ZnCdS/NiS is improved to 1.9 mmol $g^{-1}h^{-1}$ by the addition of NiS NPs. It appears that the addition of SiO_2 or NiS NPs is beneficial for the enhancement of photocatalytic activity. Therefore, when NiS NPs were deposited on the SiO_2/ZnCdS, the H_2 production rate of SiO_2/ZnCdS/NiS is as high as 8.4 mmol $g^{-1}h^{-1}$, which is 21 times higher than that of pure ZnCdS, 8.4 times of SiO_2/ZnCdS and 4.4 times of ZnCdS/NiS, indicating that structuration of the components on the SiO_2 spheres causes a synergistic effect between SiO_2 and NiS NPs, which enhances the photocatalytic performance of the system. Figure S3 shows the photocatalytic H_2 production activity of SiO_2/ZnCdS/NiS using methanol and Na_2S/Na_2SO_3 as the sacrificial agents. When methanol was used as sacrificial agent, there was no hydrogen formed. Compared with triethanolamine, the hydrogen production rate of SiO_2/ZnCdS/NiS greatly decreased to 1.9 mmol $g^{-1}h^{-1}$ when using Na_2S/Na_2SO_3 as the sacrificial agent. In addition, in order to prove the advantage of self-assembly and photo-deposition method, the H_2 production activity of samples prepared by mechanical mixture were obtained, as shown in

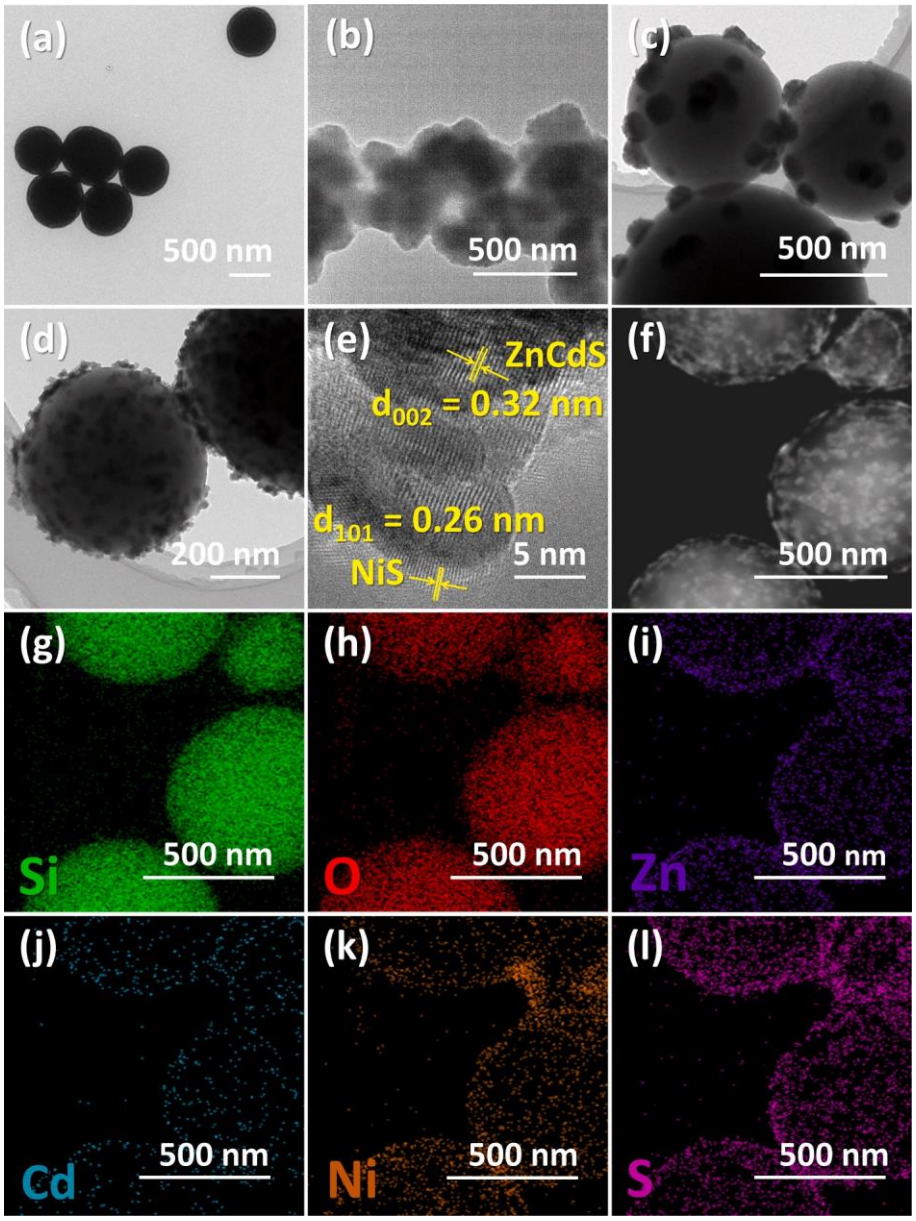

Fig. 2. TEM images of (a) SiO_2, (b) ZnCdS, (c) SiO_2/ZnCdS and (d) SiO_2/ZnCdS/NiS. HRTEM image (e), DF-TEM image (f) and EDS mappings (g-l) of SiO_2/ZnCdS/NiS.

Figure S4. The H_2 productions of SiO_2/ZnCdS-Mix and SiO_2/ZnCdS/NiS-Mix are 0.04 mmol $g^{-1}h^{1}$ and 0.63 mmol $g^{-1}h^{1}$, respectively, which are much lower than that of SiO_2/ZnCdS (1.0 mmol $g^{-1}h^{1}$) and SiO_2/ZnCdS/NiS (8.4 mmol $g^{-1}h^{1}$) prepared by self-assembly and photo-deposition method. To put the photocatalytic activity of SiO_2/ZnCdS/NiS into context, the catalyst SiO_2/ZnCdS/Pt prepared by photo-deposition method was prepared for comparison. As can be seen in Fig. 1c and Table S2, the hydrogen production of SiO_2/ZnCdS/Pt is only 3.2 mmol $g^{-1}h^{1}$, less than half than that of SiO_2/ZnCdS/NiS. A literature survey of the photocatalytic activity reported for other ZnCdS-based catalysts using metals as promoters are summarized in Table S3. As it can be seen there, the hydrogen production activities reported for these ZnCdS materials are much lower than that achieved for SiO_2/ZnCdS/NiS in the present work.

As shown in Figure S5, after four cycles, the hydrogen production activity of SiO_2/ZnCdS/NiS remains essentially constant, indicating good photocatalytic stability. The external quantum efficiency (EQE) of SiO_2/ZnCdS/NiS upon monochromatic light irradiation is shown in Table S4, and the EQE at 420 nm reaches a high value of 8.8 %.

3.2. Structure characterization

X-ray diffraction (XRD) was used to investigate the phase structure of photocatalysts. Figure S6 shows XRD patterns of the prepared five samples. There are three different distinctive diffraction peaks located at 2θ = 26.7°, 44.2° and 52.2°, corresponding to (002), (110) and (112) planes of ZnCdS, respectively. In the case of SiO_2/ZnCdS and SiO_2/ZnCdS/NiS, all peaks mentioned above can be observed, but become much weaker due to the lower crystallinity of ZnCdS and the close position of diffraction angles of SiO_2 (2θ 23°) and ZnCdS (2θ 26.7°). Compared with ZnCdS, after the addition of NiS, there is no obvious change in the XRD pattern of ZnCdS/NiS with no peaks attributable to NiS species. The lack of detectable diffraction bands of NiS can be attributed to its low loading, high dispersion and small particle size of NiS in samples ZnCdS/NiS and SiO_2/ZnCdS/NiS. Besides, the XRD pattern of SiO_2/ZnCdS/NiS after four consecutive reuses was presented

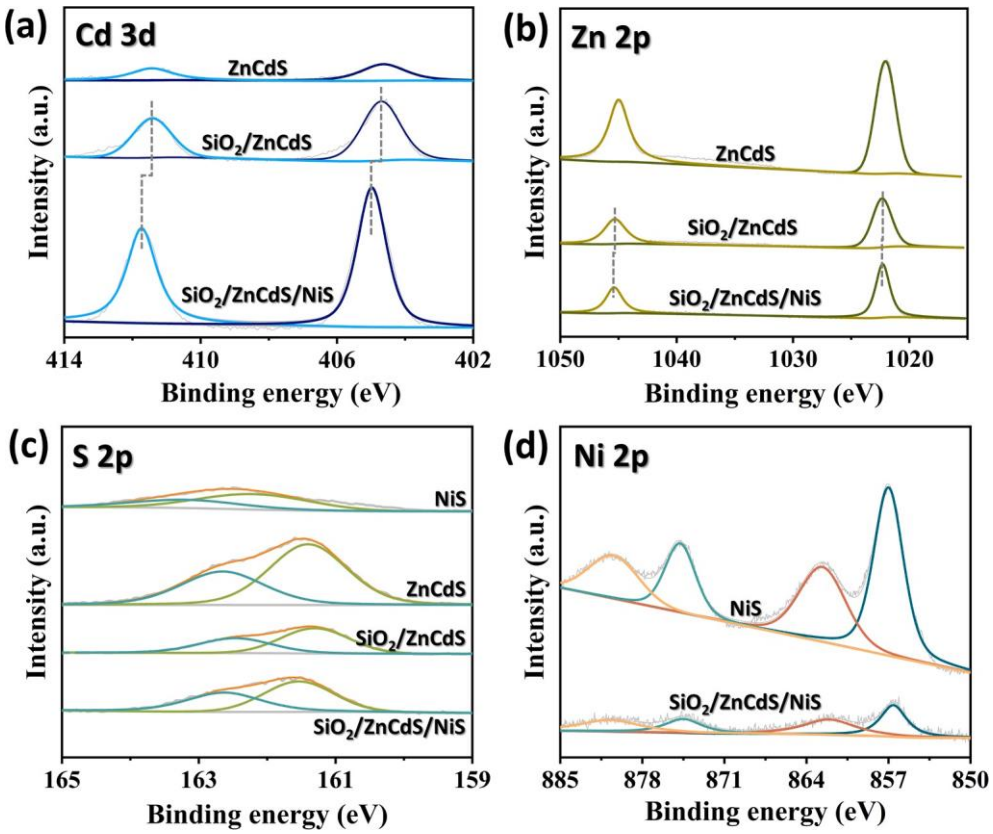

Fig. 3. High-resolution XPS spectra of Cd 3d (a), Zn 2p (b), S 2p (c) and Ni 2P (d) of different samples.

in Figure S7. It can be clearly observed that there is no obvious difference on the fresh and regenerated SiO_2/ZnCdS/NiS, indicating good stability of SiO_2/ZnCdS/NiS.

Specific surface area and pore size distribution of the samples under study were determined from the N_2 adsorption and desorption isotherms. As shown in Figure S8, all tested samples can be categorized as type IV isotherms with H3 hysteresis loops, which suggests that there are micro-mesoporous structure in the catalysts [36–38]. The specific surface area of ZnCdS, ZnCdS/NiS, SiO_2/ZnCdS and SiO_2/ZnCdS/NiS are collected in Table S5 and varies from 30.6 to 5.2 m^2/g. Among these four samples, SiO_2/ZnCdS/NiS has the smallest specific surface area, but with the highest photocatalytic hydrogen production activity, indicating that the specific surface area is not the main decisive factor affecting the catalytic activity of the series of photocatalysts. The fact that SiO_2/ZnCdS/NiS with the lowest specific surface area exhibits the highest photocatalytic activity further confirms the synergistic effect between SiO_2 and NiS NPs enhancing the H_2 production.

The microstructure and morphology of samples were investigated. As shown in Fig. 2a, SiO_2 exhibits spherical shape with a diameter of about 600–800 nm and a smooth surface. Fig. 2b displays the TEM image of pure ZnCdS, which easily undergoes agglomeration. An interplanar distance of 3.2 Å corresponding to the (002) plane of ZnCdS was measured, as shown in Figure S9, indicating the successful synthesis of ZnCdS. The TEM images clearly reveal the structure of SiO_2/ZnCdS and SiO_2/ZnCdS/NiS samples. The TEM images clearly reveal the structure of SiO_2/ZnCdS and SiO_2/ZnCdS/NiS samples. As shown in Fig. 2c, dark spheres were heterogeneously coated by smaller black hemispherical black substance in which ZnCdS located at the outer layer of SiO_2 spheres. The TEM image of SiO_2/ZnCdS/NiS was presented in Fig. 2d. SiO_2 spheres unevenly coated by ZnCdS and NiS NPs, presenting a rough surface can be clearly observed, which is different from the image of sample SiO_2/ZnCdS, suggesting the existence of NiS NPs. Meanwhile, an interplanar distance of 2.6 Å corresponding to the (101) plane of NiS is displayed in Fig. 2e, proving the NiS NPs presence. In addition, the measurement of an interplanar distance of 3.2 Å corresponding to the (002) plane of ZnCdS is also given in Fig. 2e. In addition, TEM images of SiO_2/ZnCdS with different mass ratio were shown in Figure S10. When the ratio of SiO_2 to ZnCdS is 16:1, it's hard to observe ZnCdS on the surface of the silicon spheres from Figure S10a. When increasing the proportion of ZnCdS in SiO_2/ZnCdS until SiO_2 and ZnCdS ratio of 4, in Figure S10c, SiO_2 spheres were heterogeneously coated by a larger amount of irregular black hemispherical ZnCdS, compared with that of SiO_2 and ZnCdS ratio of 8 (Fig. 2c and S10b). With the further increase of ZnCdS until SiO_2 and ZnCdS ratio of 2, as shown in Figure S10d, dark irregular spheres were unevenly coated by smaller black hemispherical black substances, indicating more ZnCdS located at the outer layer of SiO_2 spheres. Furthermore, the dark-field transmission electron microscopy (DF-TEM) image and energy dispersive spectrum (EDS) elemental mappings of SiO_2/ZnCdS/NiS with SiO_2 and ZnCdS mass ratios of 8 shown in Fig. 2f-l indicates the presence of Zn, Cd, S and Ni elements in SiO_2/ZnCdS/NiS. The distributions of the transition metal elements exhibit a spherical shape, indicating the SiO_2 spheres are coated by highly-dispersed ZnCdS, and NiS NPs. TEM images of the SiO_2/ZnCdS/NiS photocatalyst after four consecutive reuses are presented in Figure S11. Measurements of the interplanar distance of 2.6 Å corresponding to the (101) plane of NiS and 3.2 Å corresponding to the (002) plane of ZnCdS can be observed in Figure S11b, further indicating good stability of SiO_2/ZnCdS/NiS catalyst.

X-ray photoelectron spectroscopy (XPS) was employed to investigate the chemical composition of photocatalysts. The XPS spectra of Cd 3d, Zn 2p, Ni 2p and S 2p in different samples are shown in Fig. 3. As presented in Fig. 3a, there are two peaks located at binding energies of 411.7 eV and 405.0 eV, corresponding to Cd $3d_{3/2}$ and Cd $3d_{5/2}$, respectively, suggesting that Cd exists in the form of Cd^{2+} in SiO_2/ZnCdS/NiS [39–41]. And Cd exists in the form of Cd (II) in ZnCdS and SiO_2/ZnCdS as well. Fig. 3b displays the XPS spectrum of Zn 2p, showing

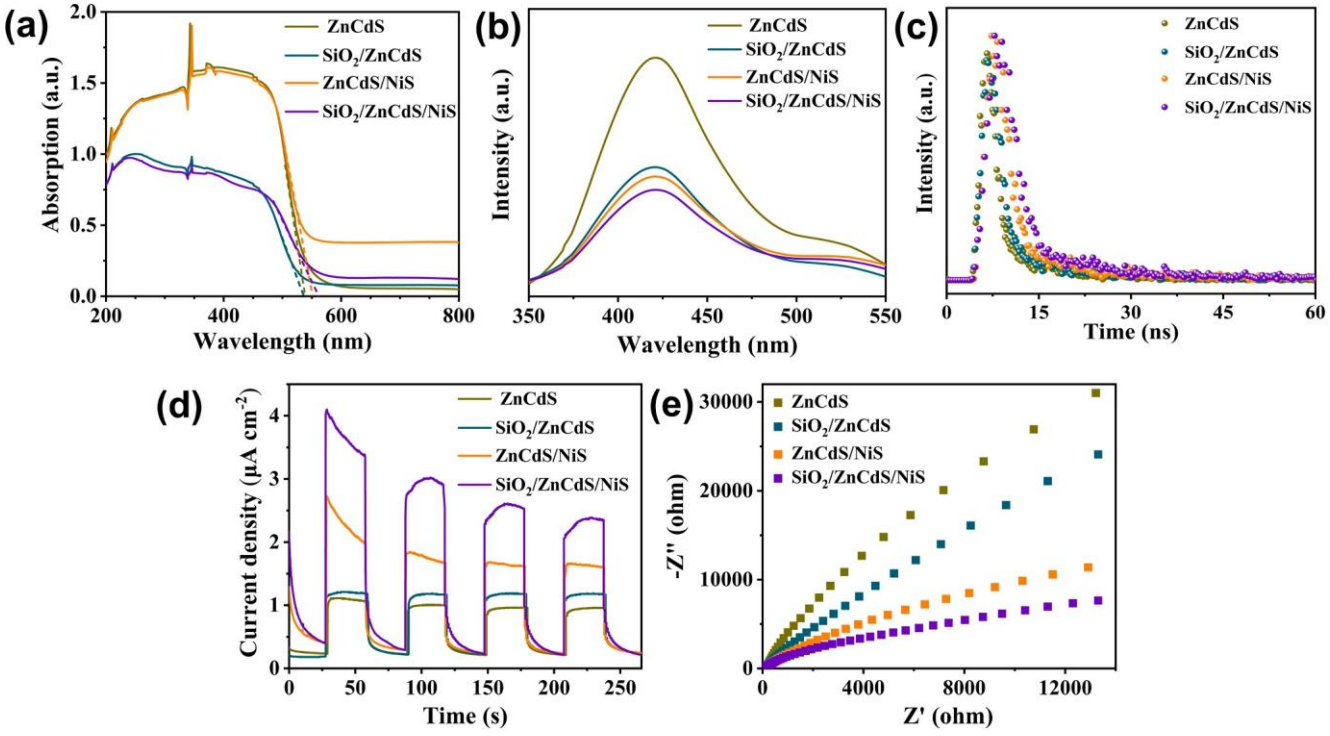

Fig. 4. (a) UV–vis diffuse reflectance spectra, (b) photoluminescence spectra, (c) time-resolved fluorescence spectra, (d) photocurrent responses under visible light irradiation and (e) electrochemical impedance spectra of catalysts.

two peaks at binding energies of 1045.3 eV and 1022.3 eV, are assigned to the Zn $2p_{1/2}$ and Zn $2p_{3/2}$, respectively, indicating that Zn exists in the form of Zn^{2+} in SiO_2/ZnCdS/NiS [42]. Again, it is proven that Zn stays in the form of Zn (II) in ZnCdS and SiO_2/ZnCdS. As shown in Fig. 3c, two peaks appearing at binding energies of 162.7 eV and 161.6 eV can be ascribed to S $2p_{1/2}$ and S $2p_{3/2}$, respectively, suggesting the element S in the compound exists in the form of S^{2-}[43,44]. The high-resolution Ni 2p spectrum given in Fig. 3d can be divided into four peaks. Two distinct peaks at binding energies of 856.6 and 874.5 eV correspond to Ni $2p_{3/2}$ and Ni $2p_{1/2}$, which indicates the appearance of Ni (II) and is consistent with the formation of NiS. And two satellites are located at 861.9 eV and 880.4 eV [45,46]. It can be concluded that Zn, Cd and S exists in the form of Zn^{2+}, Cd^{2+} and S^{2-} in photocatalysts of ZnCdS, SiO_2/ZnCdS and SiO_2/ZnCdS/NiS. Compared with SiO_2/ZnCdS/NiS, the binding energy of Cd 3d, Zn 2p in SiO_2/ZnCdS shifts to lower energy, which suggests the electron shift from ZnCdS to NiS when NiS as co-catalyst [47,48].

3.3. Optical and electrochemical properties of ZnCdS, ZnCdS/NiS, SiO_2/ZnCdS and SiO_2/ZnCdS/NiS catalysts

Ultraviolet–visible (UV–vis) spectroscopy was employed to study the optical properties of ZnCdS, ZnCdS/NiS, SiO_2/ZnCdS and SiO_2/ZnCdS/NiS. Fig. 4a shows the UV–vis spectra of as-prepared samples, demonstrating all the catalysts have photoabsorption in the visible region. Compared with ZnCdS, there is no shift on the absorption edge of SiO_2/ZnCdS, while that of ZnCdS/NiS and SiO_2/ZnCdS/NiS have a significant red shift, which should arise from the light absorption of NiS NPs. However, the red shift for SiO_2/ZnCdS/NiS is larger than that of ZnCdS/NiS due to the scattered light absorption of NiS NPs in the near-field of SiO_2 spheres [20,21,49].

Photoluminescence (PL) spectroscopy was used for a better understanding of the relative charge separation efficiency of these photocatalysts. The higher PL intensity indicates the higher efficiency of electron-hole pair recombination [50]. As shown in Fig. 4b, the emission spectra of these photocatalysts are the same, but with considerably different intensities, especially higher for ZnCdS. The PL intensity of these samples follows the order of ZnCdS > SiO_2/ZnCdS > ZnCdS/NiS > SiO_2/ZnCdS/NiS. Compared with only introducing SiO_2, deposition of NiS NPs inhibits the recombination of electrons and holes with higher efficiency, probably due to the easy migration of photogenerated electrons to NiS NPs, meanwhile the holes remain in ZnCdS. In Fig. 4c, time-resolved fluorescence (TRF) measurements agrees with the migration of photogenerated electrons to NiS, the emission becoming longer lived. The signal decays of all photocatalysts could be adequately fitted to a three consecutive first-order function. The three lifetimes and the corresponding percentage of charge carriers are listed in Table 1, in which τ_1, τ_2, and τ_v represent the radiation lifetime, the lifetime of the non-radiation phase and the average lifetime, respectively [51]. The values of τ_1, τ_2, and τ_v of these photocatalysts follow the order of ZnCdS < SiO_2/ZnCdS < ZnCdS/NiS < SiO_2/ZnCdS/NiS, showing the effect of NiS slowing down electron/hole recombination. The longest emission time of SiO_2/ZnCdS/NiS indicates a highest probability of charge carriers in participating in the photocatalytic reaction. Besides charge transfer, energy transfer processes are quantitatively measured by the energy transfer rate constant (K_{ENT}) and energy transfer efficiency (Φ_{ENT}). According to the values of K_{ENT} and Φ_{ENT} in Table 1, SiO_2/ZnCdS/NiS with highest value indicates that the structural arrangement of ZnCdS/NiS on the SiO_2 surface is favourable to promote the energy transfer. The results of PL and TRF illustrate that the synergistic effect of SiO_2 and NiS NPs effectively inhibits the electron-hole recombination and considerably promotes charge transfer, thereby enhancing the photocatalytic

Table 1
Parameters obtained from time-resolved PL decay curves.

Samples	τ_1 (ns) (Rel.%)	τ_2 (ns) (Rel.%)	τ_v (ns)	K_{ENT}	Φ_{ENT}
ZnCdS	4.12 (83.75)	11.23 (16.25)	6.58	0.154	0.0374
SiO_2/ZnCdS	4.32 (80.15)	15.65 (19.85)	9.68	0.168	0.0389
ZnCdS/NiS	4.48 (72.85)	21.35 (27.15)	15.27	0.176	0.0393
SiO_2/ZnCdS/NiS	4.68 (66.35)	35.75 (33.65)	29.38	0.186	0.0397

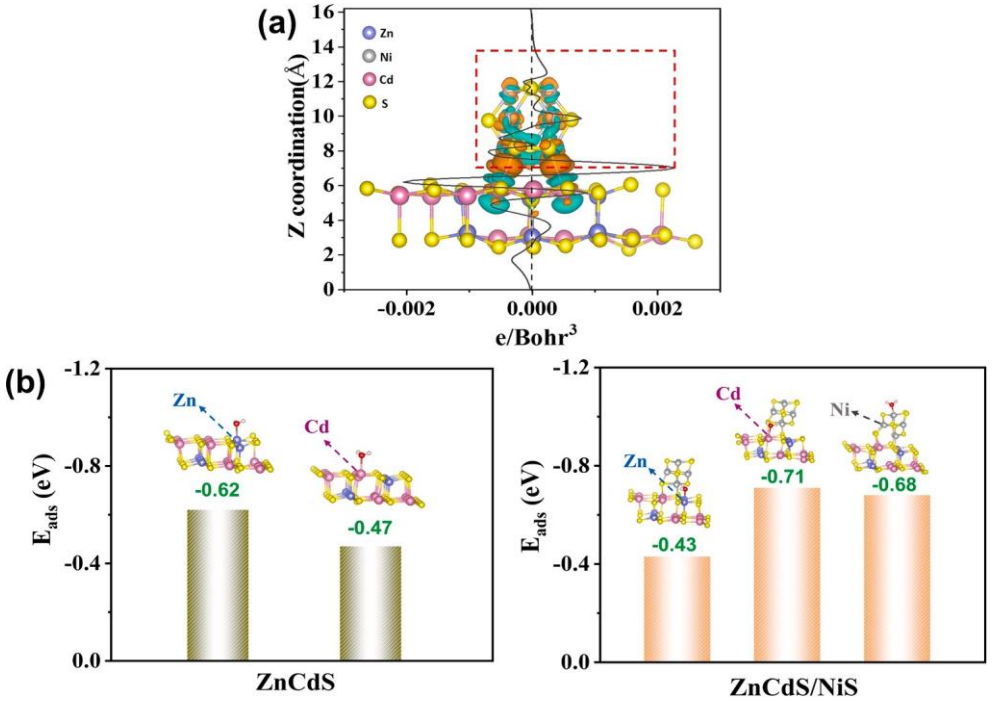

Fig. 5. (a) The charge distribution and density of ZnCdS/NiS, (b) the adsorption energies of a single water molecule on different sites for ZnCdS and ZnCdS/NiS.

performance of the photocatalyst.

Photoelectrochemical experiments were also carried out to investigate the separation of photogenerated charges and the migration of electrons to the electrode. Comparing the photocurrent response of these four photocatalysts, as shown in Fig. 4d, SiO_2/ZnCdS/NiS with the highest photocurrent density confirms the advantage of the use of SiO_2 spheres as supports and deposition of NiS NPs co-catalyst to enhance the separation of electron-hole pairs [52–54]. In addition, the electrochemical impedance spectroscopy (EIS) was further used to determine the contribution of the independent components to the

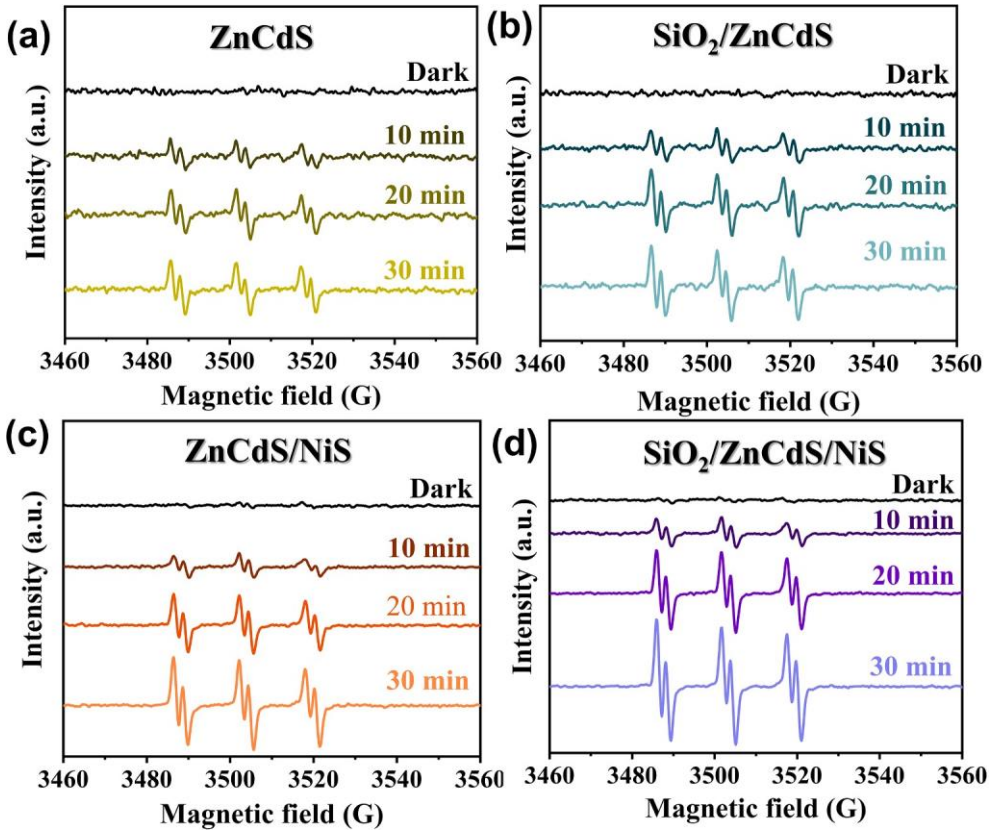

Fig. 6. EPR spectra of H• trapping by POBN (POBN-H•) for (a) ZnCdS, (b) SiO_2/ZnCdS (c) ZnCdS/NiS, and (d) SiO_2/ZnCdS/NiS.

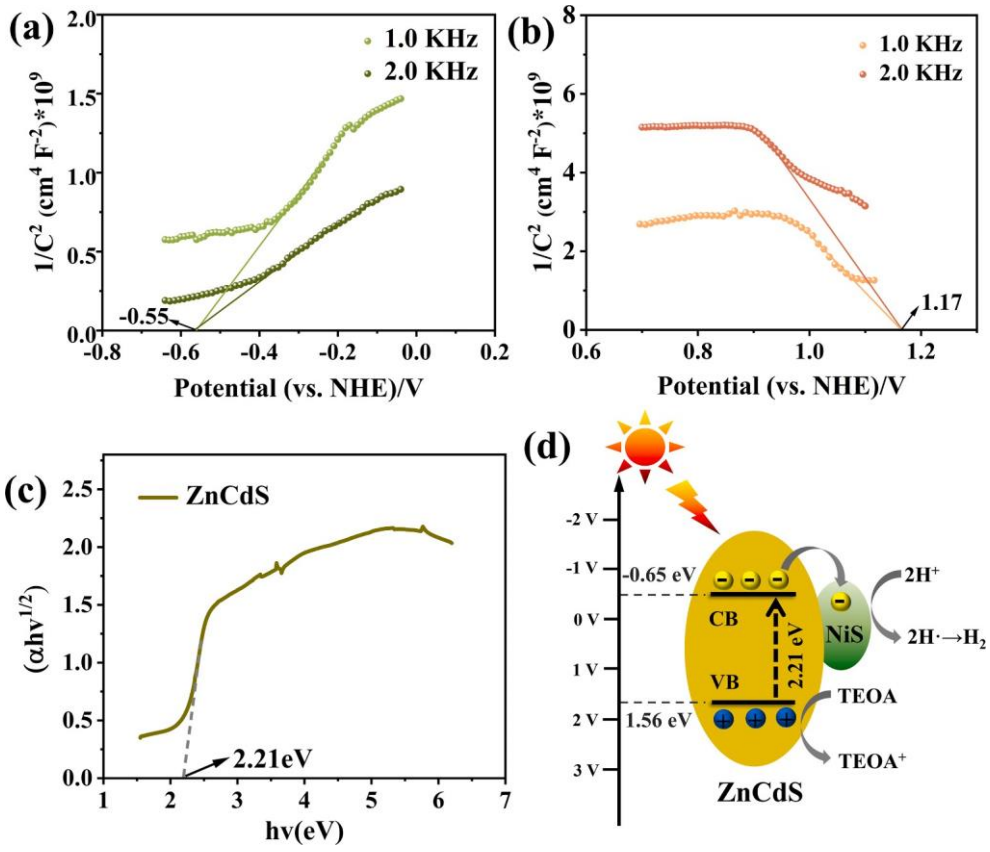

Fig. 7. Mott-Schottky plot of (a) ZnCdS, (b) NiS (c) Plot of $(\alpha h\upsilon)^{-2}$ versus ($h\upsilon$) for band-gap calculation of ZnCdS (d) Schematic diagram for the promotion effect of NiS on the photocatalytic H_2 evolution of ZnCdS under visible sunlight.

photoelectrochemical properties of the different materials. The arc radius of the semicircular part of the Nyquist plot reflects the surface reaction rate and the magnitude of the electrode resistance. The smaller the radius of the arc, the higher the efficiency of the charge transfer from the photocatalyst to the electrolyte solution [55,56]. Fig. 4e shows that pure ZnCdS exhibits the largest radius and SiO_2/ZnCdS/NiS the smallest. This indicates that the loading of ZnCdS on SiO_2 and the deposition of NiS NPs can accelerate the charge transfer on the catalyst to the solution.

3.4. DFT calculations

After confirming that NiS NPs not only effectively inhibit electron-hole recombination and also considerably promote charge transfer, the first-principles density functional theory (DFT) was used to further investigate the catalytic mechanism. The charge distribution and density of ZnCdS/NiS are displayed in Fig. 5a, in which the blue and orange parts represent the depletion and accumulation of electrons, respectively. The redistribution of electron density for ZnCdS/NiS, with electron depletion mainly on the ZnCdS surface and electron accumulation on NiS. The calculations indicate that electron accumulation on NiS is beneficial for its role as reaction site, promoting the hydrogen evolution. In addition, for a better understanding of the interaction between the ZnCdS or ZnCdS/NiS with water molecules, the adsorption energies of ZnCdS and ZnCdS/NiS for one water molecule was calculated and the results presented in Fig. 5b. The more negative value the adsorption energy is, the stronger the water adsorption is. Comparison of the adsorption energies of different adsorption sites on ZnCdS and ZnCdS/NiS for a single water molecule leads to the conclusion that after deposition of NiS, the water adsorption capacity of ZnCdS/NiS becomes enhanced, which should be favorable for photocatalytic water decomposition.

3.5. Photocatalytic mechanism of H_2 production

Electron paramagnetic resonance (EPR) spectroscopy was used to detect free radicals as reaction intermediates generated in the photocatalytic reaction. Fig. 6 shows the EPR spectra of four ZnCdS materials by performing the photocatalytic H_2 production in the presence of POBN as a spin-trapping agent. The peaks of POBN-H adducts with different intensities were recorded for all photocatalysts under visible light irradiation, confirming that H• radicals are intermediate species in the process of photocatalytic hydrogen production. The peak intensities of POBN-H• for the four photocatalysts follow the order of ZnCdS < SiO_2/ZnCdS < ZnCdS/NiS < SiO_2/ZnCdS/NiS, which is consistent with their hydrogen production activity, suggesting the formation rate of H• radicals is promoted under the synergistic effect of SiO_2 and NiS NPs, thereby enhancing the photocatalytic hydrogen evolution performance.

The band potentials of ZnCdS was investigated. The plot of $(\alpha h\upsilon)^2$ vs $h\upsilon$ is given in Fig. 7c, the extrapolation of the linear region shows the optical band-gap E_g of the ZnCdS is about 2.21 eV. The Mott-Schottky plots in Fig. 7a and 7b show that ZnCdS is a *n*-type semiconductor with a Femi level of 0.55 V(vs NHE), and the Femi level of NiS is 1.17 V (vs NHE) [57]. ZnCdS with a flat band potential (V_{fb}) of 0.55 V (vs NHE), considering that the V_{fb} of *n*-type semiconductor is usually ~0.1 V more positive than the ECB, the conduction band (CB) edge of ZnCdS was estimated to be 0.65 (vs NHE). Thus, based on the DRS data for the optical bandgap (E_g 2≅21 eV) and the equation, E_g E_{VB}-E⊂⊨B, the valence band (VB) top of ZnCdS was determined to be 1.56 eV. Ac- cording to the DFT calculation and EPR results, the reaction mechanism can be inferred as presented in Fig. 7d. The Fermi level of ZnCdS is located higher than that of NiS, indicating that electrons from NiS are excited into the CB of ZnCdS upon irradiation, which is also confirmed by the DFT calculation. Then the electrons will react with H^+ from H_2O

to produce H_2 through the intermediacy of H· (supported by EPR results) and the holes left on VB will be consumed by sacrificial agents. This process effectively separated electrons and holes and inhibited their recombination, thus greatly improving the activity of photocatalytic hydrogen production.

Based on the above discussion, the improvement of SiO_2/ZnCdS/NiS with enhanced photocatalytic activity can be attributed to the following reasons. (1) NiS NPs promote the scattered light absorption in the near field of SiO_2 spheres, thereby increasing the utilization of light, generating hot electrons on the photocatalyst. (2) the synergistic effect of SiO_2 and NiS NPs can effectively inhibit the electron-hole recombination and accelerate the charge transfer, in which the photogenerated electrons can easily migrate to NiS NPs, meanwhile the holes remain in ZnCdS, thereby enhancing the photocatalytic performance. (3) Electrons accumulation is realized by NiS deposition, that is beneficial for further providing electrons to H^+ from water, therefore promoting hydrogen evolution [58]. In addition, loading of NiS NPs on ZnCdS improves the water adsorption capacity of photocatalyst, being more conducive to the photocatalytic water decomposition.

4. Conclusions

In this work, a highly efficient noble metal-free photocatalyst SiO_2/ZnCdS/NiS has been successfully prepared through the photodeposition method, of which the hydrogen production activity under visible light is as high as 8.4 mmol $g^{-1}h^{1}$, 8.4 times of SiO_2/ZnCdS and 4.4 times of ZnCdS/NiS, indicating that the synergistic effect of SiO_2 and NiS NPs can effectively inhibit the electron-hole recombination and accelerate the charge transfer, thereby enhancing the photocatalytic performance. Apparent quantum efficiencies at the visible range edge as high as 8.8 % for H_2 evolution have been reached. The experimental results have been rationalized by DFT calculations that show that the presence of NiS NPs improves the water adsorption capacity of photocatalyst, being more conducive to the photocatalytic hydrogen production. Meanwhile, NiS becomes an electron accumulation site, this fact together with favorable water adsorption being beneficial for providing electrons to H^+, therefore promoting hydrogen evolution. Excitingly, the photocatalytic activity of SiO_2/ZnCdS/NiS is 2.6 times that of SiO_2/ZnCdS/Pt, indicating the importance of design to optimize photocatalyst for hydrogen production.

CRediT authorship contribution statement

Ke Liu: Investigation, Data curation, Methodology, Validation, Writing – original draft. **Shan Yang:** Resources, Validation, Supervision, Writing – review & editing. **Wei Li:** Methodology, Writing – review & editing. **Yifan Wang:** Validation, Writing – review & editing. **Chuanzhi Sun:** Conceptualization, Methodology, Resources, Funding acquisition. **Lu Peng:** Writing – review & editing. **Hermenegildo Garcia:** Supervision.

Declaration of Competing Interest

The authors declare that they have no known competing financial interests or personal relationships that could have appeared to influence the work reported in this paper.

Data availability

Data will be made available on request.

Acknowledgements

This work was supported by the National Natural Science Foundation of China (21976111), Shandong Provincial Natural Science Foundation (ZR2019MB052).

Appendix A. Supplementary data

Supplementary data to this article can be found online

References

[1] Fujishima A, Honda K. Electrochemical photolysis of water at a semiconductor electrode. Nature 1972;238(5358):37–8. https://doi.org/10.1038/238037a0.
[2] Zheng M, Ding Y, Yu L, Du X, Zhao Y. In Situ Grown Pristine Cobalt Sulfide as Bifunctional Photocatalyst for Hydrogen and Oxygen Evolution. Adv Funct Mater 2017;27(11):1605846. https://doi.org/10.1002/adfm.201605846.
[3] Sun Y, Liu C, Grauer DC, Yano J, Long JR, Yang P, et al. Electrodeposited cobalt-sulfide catalyst for electrochemical and photoelectrochemical hydrogen generation from water. J Am Chem Soc 2013;135(47):17699–702.
[4] Liao L, Zhang Q, Su Z, Zhao Z, Wang Y, Li Y, et al. Efficient solar water-splitting using a nanocrystalline CoO photocatalyst. Nat Nanotechnol 2014;9(1):69–73.
[5] Rockafellow EM, Stewart LK, Jenks WS. Is sulfur-doped TiO_2 an effective visible light photocatalyst for remediation? Appl Catal B: Environ 2009;91(1–2):554–62. https://doi.org/10.1016/j.apcatb.2009.06.027.
[6] Han C, Pelaez M, Likodimos V, Kontos AG, Falaras P, O'Shea K, et al. Innovative visible light-activated sulfur doped TiO_2 films for water treatment. Appl Catal B: Environ 2011;107(1-2):77–87.
[7] Wang J, Chen J, Wang P, Hou J, Wang C, Ao Y. Robust photocatalytic hydrogen evolution over amorphous ruthenium phosphide quantum dots modified g-C_3N_4 nanosheet. Applied Catalysis B: Environ 2018;239:578–85. https://doi.org/10.1016/j.apcatb.2018.08.048.
[8] Yang H, Dai K, Zhang J, Dawson G. Inorganic-organic hybrid photocatalysts: Syntheses, mechanisms, and applications. Chin J Catal 2022;43(8):2111–40.
[9] Jin Z, Liu Y, Hao X. Self-assembly of zinc cadmium sulfide nanorods into nanoflowers with enhanced photocatalytic hydrogen production activity. J Colloid Interface Sci 2020;567:357–68. https://doi.org/10.1016/j.jcis.2020.02.024.
[10] Song L, liu D, Zhang S, Wei J. WO_3 cocatalyst improves hydrogen evolution capacity of ZnCdS under visible light irradiation. Int J Hydrogen Energy 2019;44(31):16327–35.
[11] Wu J-C, Zheng J, Zacherl CL, Wu P, Liu Z-K, Xu R. Hybrid Functionals Study of Band Bowing, Band Edges and Electronic Structures of $Cd_{1-x}Zn_xS$ Solid Solution. J Phys Chem C 2011;115(40):19741–8. https://doi.org/10.1021/jp204799q.
[12] Xing C, Zhang Y, Yan W, Guo L. Band structure-controlled solid solution of $Cd_{1-x}Zn_xS$ photocatalyst for hydrogen production by water splitting. Int J Hydrogen Energy 2006;31(14):2018–24. https://doi.org/10.1016/j.ijhydene.2006.02.003.
[13] Gogoi G, Keene S, Patra AS, Sahu TK, Ardo S, Qureshi M. Hybrid of g-C_3N_4 and MoS_2 Integrated onto $Cd_{0.5}Zn_{0.5}S$: Rational Design with Efficient Charge Transfer for Enhanced Photocatalytic Activity. ACS Sustain Chem Eng 2018;6(5):6718–29. https://doi.org/10.1021/acssuschemeng.8b00512.
[14] Zhao X, Feng J, Liu J, Shi W, Yang G, Wang G-C, et al. An Efficient, Visible-Light-Driven, Hydrogen Evolution Catalyst NiS/Zn_x $Cd_{1-x}S$ Nanocrystal Derived from a Metal-Organic Framework. Angew Chem Int Ed Engl 2018;57(31):9790–4.
[15] Han Z, Chen G, Li C, Yu Y, Zhou Y. Preparation of 1D cubic $Cd_{0.8}Zn_{0.2}S$ solid-solution nanowires using levelling effect of TGA and improved photocatalytic H_2-production activity. J Mate Chem A 2015;3(4):1696–702. https://doi.org/10.1039/c4ta05615a.
[16] Jiang D, Sun Z, Jia H, Lu D, Du P. A cocatalyst-free CdS nanorod/ZnS nanoparticle composite for high-performance visible-light-driven hydrogen production from water. J Mate Chem A 2016;4(2):675–83. https://doi.org/10.1039/c5ta07420g.
[17] Su Y, Zhang Z, Liu H, Wang Y. $Cd_{0.2}Zn_{0.8}S$@UiO-66-NH_2 nanocomposites as efficient and stable visible-light-driven photocatalyst for H_2 evolution and CO_2 reduction. Appl Catal B: Environ 2017;200:448–57. https://doi.org/10.1016/j.apcatb.2016.07.032.
[18] Chen Y, Guo L. Highly efficient visible-light-driven photocatalytic hydrogen production from water using $Cd_{0.5}Zn_{0.5}S$/TNTs (titanate nanotubes) nanocomposites without noble metals. J Mater Chem 2012;22(15):7507–14. https://doi.org/10.1039/c2jm16797b.
[19] Yao L, Wei D, Ni Y, Yan D, Hu C. Surface localization of CdZnS quantum dots onto 2D g-C_3N_4 ultrathin microribbons: Highly efficient visible light-induced H_2-generation. Nano Energy 2016;26:248–56. https://doi.org/10.1016/j.nanoen.2016.05.031.
[20] Zhang N, Qi M-Y, Yuan L, Fu X, Tang Z-R, Gong J, et al. Broadband Light Harvesting and Unidirectional Electron Flow for Efficient Electron Accumulation for Hydrogen Generation. Angew Chem Int Ed Engl 2019;58(29):10003–7.
[21] Zhang N, Han C, Xu Y-J, Foley IV JJ, Zhang D, Codrington J, et al. Near-field dielectric scattering promotes optical absorption by platinum nanoparticles. Nat Photonics 2016;10(7):473–82.
[22] Yan H, Yang J, Ma G, Wu G, Zong Xu, Lei Z, et al. Visible-light-driven hydrogen production with extremely high quantum efficiency on Pt–PdS/CdS photocatalyst. J Catal 2009;266(2):165–8.
[23] Murdoch M, Waterhouse GIN, Nadeem MA, Metson JB, Keane MA, Howe RF, et al. The effect of gold loading and particle size on photocatalytic hydrogen production from ethanol over Au/TiO_2 nanoparticles. Nat Chem 2011;3(6):489–92.
[24] Onsuratoom S, Puangpetch T, Chavadej S. Comparative investigation of hydrogen production over Ag-, Ni-, and Cu-loaded mesoporous-assembled TiO_2–ZrO_2 mixed oxide nanocrystal photocatalysts. Chem Eng J 2011;173(2):667–75. https://doi.org/10.1016/j.cej.2011.08.016.

[25] Sayed FN, Jayakumar OD, Sasikala R, Kadam RM, Bharadwaj SR, Kienle L, et al. Photochemical Hydrogen Generation Using Nitrogen-Doped TiO_2–Pd Nanoparticles: Facile Synthesis and Effect of Ti^{3+} Incorporation. J Phys Chem C 2012;116(23):12462–7.

[26] Liang Z, Dong X. Fabrication of layered Fe_2P-$Cd_{0.5}Zn_{0.5}S$ nanoparticles with a reverse heterojunction for enhanced photocatalytic hydrogen evolution. J Colloid Interface Sci 2021;583:196–203. https://doi.org/10.1016/j.jcis.2020.09.042.

[27] Zhang D, Peng L, Liu K, Garcia H, Sun C, Dong L. Cobalt nanoparticle with tunable size supported on nitrogen-deficient graphitic carbon nitride for efficient visible light driven H_2 evolution reaction. Chem Eng J 2020;381:122576. https://doi.org/10.1016/j.cej.2019.122576.

[28] Zheng X, Liu K, Chen L, He H, Chen L, Sun C. CoO_x Particles in Polymeric N-Doped Carbon Nanotube Applied for Photocatalytic H_2 or Electrocatalytic O_2 Evolution. Polymers (Basel) 2019;11(11):1836. https://doi.org/10.3390/polym11111836.

[29] Sun C, Zhang H, Liu H, Zheng X, Zou W, Dong L, et al. Enhanced activity of visible-light photocatalytic H_2 evolution of sulfur-doped g-C_3N_4 photocatalyst via nanoparticle metal Ni as cocatalyst. Appl Catal B: Environ 2018;235:66–74.

[30] Li Y, Zhu S, Liang Y, Li Z, Wu S, Chang C, et al. One-step synthesis of Mo and S co-doped porous g-C_3N_4 nanosheets for efficient visible-light photocatalytic hydrogen evolution. Appl Surf Sci 2021;536:147743.

[31] Hu T, Dai K, Zhang J, Chen S. Noble-metal-free Ni_2P modified step-scheme $SnNb_2O_6$/CdS-diethylenetriamine for photocatalytic hydrogen production under broadband light irradiation. Applied Catalysis B: Environ 2020;269:118844. https://doi.org/10.1016/j.apcatb.2020.118844.

[32] Wang J, Wang P, Wang C, Ao Y. In-situ synthesis of well dispersed CoP nanoparticles modified CdS nanorods composite with boosted performance for photocatalytic hydrogen evolution. Int J Hydrogen Energ 2018;43(32):14934–43. https://doi.org/10.1016/j.ijhydene.2018.06.101.

[33] He B, Bie C, Fei X, Cheng B, Yu J, Ho W, et al. Enhancement in the photocatalytic H_2 production activity of CdS NRs by Ag_2S and NiS dual cocatalysts. Applied Catalysis B: Environ 2021;288:119994.

[34] Liu Y, Hao X, Hu H, Jin Z. High Efficiency Electron Transfer Realized over NiS_2/$MoSe_2$ S-Scheme Heterojunction in Photocatalytic Hydrogen Evolution. Acta Physico Chimica Sinica 2021;37:2008030. https://doi.org/10.3866/PKU.WHXB202008030.

[35] Wang J, Wang P, Hou J, Qian J, Wang C, Ao Y. In situ surface engineering of ultrafine Ni_2P nanoparticles on cadmium sulfide for robust hydrogen evolution. Catal. Sci Technol 2018;8(21):5406–15. https://doi.org/10.1039/c8cy00519b.

[36] Zhu Q, Sun Y, Xu S, Li Y, Lin X, Qin Y. Rational design of 3D/2D In_2O_3 nanocube/$ZnIn_2S_4$ nanosheet heterojunction photocatalyst with large-area "high-speed channels" for photocatalytic oxidation of 2,4-dichlorophenol under visible light. J Hazard Mater 2020;382:121098. https://doi.org/10.1016/j.jhazmat.2019.121098.

[37] Jian S, Tian Z, Hu J, Zhang K, Zhang L, Duan G, et al. Enhanced visible light photocatalytic efficiency of La-doped ZnO nanofibers via electrospinning-calcination technology. Adv Powder Mater 2022;1(2):100004.

[38] Huo S, Gao W, Zhou P, Deng Z, Han Z, Cui X, et al. Magnetic porous carbon composites for rapid and highly efficient degradation of organic pollutants in water. Adv Powder Mater 2022;1(3):100028.

[39] Guo H, Ding J, Wan S, Wang Y, Zhong Q. Highly efficient CH_3OH production over $Zn_{0.2}Cd_{0.8}S$ decorated g-C_3N_4 heterostructures for the photoreduction of CO_2. Appl Surf Sci 2020;528:146943. https://doi.org/10.1016/j.apsusc.2020.146943.

[40] Zhang W, Xu R. Surface engineered active photocatalysts without noble metals: CuS–$Zn_xCd_{1-x}S$ nanospheres by one-step synthesis. Int J Hydrogen Energ 2009;34(20):8495–503. https://doi.org/10.1016/j.ijhydene.2009.08.041.

[41] Dai K, Lv J, Zhang J, Zhu G, Geng L, Liang C. Efficient Visible-Light-Driven Splitting of Water into Hydrogen over Surface-Fluorinated Anatase TiO2 Nanosheets with Exposed 001 Facets/Layered CdS–Diethylenetriamine Nanobelts. ACS Sustain Chem Eng 2018;6(10):12817–26. https://doi.org/10.1021/acssuschemeng.8b02064.

[42] Gong H, Zhang X, Wang G, Liu Y, Li Y, Jin Z. Dodecahedron ZIF-67 anchoring ZnCdS particles for photocatalytic hydrogen evolution. Mol Catal 2020;485:110832. https://doi.org/10.1016/j.mcat.2020.110832.

[43] Luo Z, Zhao X, Zhang H, Jiang Y. $Zn_{0.3}Cd_{0.7}S$ nanorods loaded with noble-metal-free Ni_3C co-catalyst enhancing photocatalytic hydrogen evolution. Appl Catal A-Gen 2019;582:117115. https://doi.org/10.1016/j.apcata.2019.117115.

[44] Lee DJ, Mohan Kumar G, Ilanchezhiyan P, Lee JC, Ryu SR, Kang TW. Vertically aligned ZnCdS nanowire arrays/P3HT heterojunctions for solar cell applications. J Colloid Interface Sci 2017;487:73–9. https://doi.org/10.1016/j.jcis.2016.10.006.

[45] Hu M, Laghari M, Cui B, Xiao B, Zhang B, Guo D. Catalytic cracking of biomass tar over char supported nickel catalyst. Energy 2018;145:228–37. https://doi.org/10.1016/j.energy.2017.12.096.

[46] Prieto P, Nistor V, Nouneh K, Oyama M, Abd-Lefdil M, Díaz R. XPS study of silver, nickel and bimetallic silver–nickel nanoparticles prepared by seed-mediated growth. Appl Surf Sci 2012;258(22):8807–13. https://doi.org/10.1016/j.apsusc.2012.05.095.

[47] Yang H, Zhang Jf, Dai K. Organic amine surface modified one-dimensional $CdSe_{0.8}S_{0.2}$-diethylenetriamine/two-dimensional $SnNb_2O_6$ S-scheme heterojunction with promoted visible-light-driven photocatalytic CO_2 reduction. Chinese Journal of Catalysis 2022;43(2):255-64. https://doi: 10.1016/S1872-2067(20)63784-6.

[48] Li X, Wang Z, Zhang J, Dai K, Fan K, Dawson G. Branch-like Cd Zn1-Se/Cu_2O@Cu step-scheme heterojunction for CO_2 photoreduction. Materials Today Physics 2022;26:100729. https://doi.org/10.1016/j.mtphys.2022.100729.

[49] Zhang N, Han C, Fu X, Xu Y-J. Function-Oriented Engineering of Metal-Based Nanohybrids for Photoredox Catalysis: Exerting Plasmonic Effect and Beyond. Chem 2018;4(8):1832–61. https://doi.org/10.1016/j.chempr.2018.05.005.

[50] Li X, Zhang J, Dai K, Fan K, Liang C. $Cd_3(C_3N_3S_3)_2$ Polymer/Sn Schottky Heterojunction for Broadband-Solar Highly Selective Photocatalytic CO_2 Reduction. Solar RRL 2021;5(12):2100788. https://doi.org/10.1002/solr.202100788.

[51] Liu Ke, Peng Lu, Zhen P, Chen L, Song S, Garcia H, et al. ZnCdS Dotted with Highly Dispersed Pt Supported on SiO_2 Nanospheres Promoting Photocatalytic Hydrogen Evolution. J Phys Chem C 2021;125(27):14656–65.

[52] Yuan Y-J, Shen Z-K, Wang P, Li Z, Pei L, Zhong J, et al. Metal-free broad-spectrum PTCDA/g-C_3N_4 Z-scheme photocatalysts for enhanced photocatalytic water oxidation. Appl Catal B: Environ 2020;260:118179.

[53] Zhao G, Ma W, Wang X, Xing Y, Hao S, Xu X. Self-water-absorption-type two-dimensional composite photocatalyst with high-efficiency water absorption and overall water-splitting performance. Adv Powder Mater 2022;1(2):100008. https://doi.org/10.1016/j.apmate.2021.09.008.

[54] Mei F, Li Z, Dai K, Zhang J, Liang C. Step-scheme porous g-C_3N_4/$Zn_{0.2}Cd_{0.8}S$-DETA composites for efficient and stable photocatalytic H_2 production. Chin J Catal 2020;41(1):41–9.

[55] Xia J, Di J, Yin S, Xu H, Zhang J, Xu Y, et al. Facile fabrication of the visible-light-driven Bi_2WO_6/BiOBr composite with enhanced photocatalytic activity. RSC Adv 2014;4(1):82–90.

[56] Hu X, Li Y, Wei X, Wang L, She H, Huang J, et al. Preparation of double-layered Co Ci/NiFeOOH co-catalyst for highly meliorated PEC performance in water splitting. Adv Powder Mater 2022;1(3):100024.

[57] Zhang W, Xing P, Zhang J, Chen Lu, Yang J, Hu X, et al. Facile preparation of novel nickel sulfide modified $KNbO_3$ heterojunction composite and its enhanced performance in photocatalytic nitrogen fixation. J Colloid Interface Sci 2021;590:548–60.

[58] Wageh S, Ahmed A, Al-Ghamdi XQL. Core-Shell Au@NiS_{1+x} Cocatalyst for Excellent TiO_2 Photocatalytic H_2 Production. Acta Phys -Chim Sin 2022;38(7):2202001. https://doi.org/10.3866/PKU.WHXB202202001.